Direct Evidence of Stacking Disorder in the Mixed Ionic-Electronic Conductor $Sr_4Fe_6O_{12+\delta}$
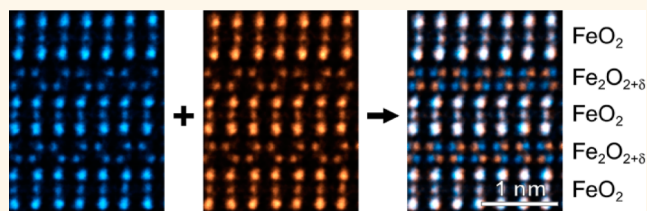
Marta D. Rossell,[†,*] Artem M. Abakumov,[‡] Quentin M. Ramasse,[§] and Rolf Erni[†]

[†]Electron Microscopy Center, Empa, Swiss Federal Laboratories for Materials Science and Technology, Überlandstrasse 129, 8600 Dübendorf, Switzerland, [‡]EMAT, University of Antwerp, Groenenborgerlaan 171, B-2020 Antwerp, Belgium, and [§]SuperSTEM Laboratory, STFC Daresbury Campus, Keckwick Lane, Warrington, WA4 4AD, United Kingdom

ABSTRACT Determining the structure-to-property relationship of materials becomes particularly challenging when the material under investigation is dominated by defects and structural disorder. Knowledge on the exact atomic arrangement at the defective structure is required to understand its influence on the functional properties. However, standard diffraction techniques deliver structural information that is averaged over many unit cells. In particular,

information about defects and order—disorder phenomena is contained in the coherent diffuse scattering intensity which often is difficult to uniquely interpret. Thus, the examination of the local disorder in materials requires a direct method to study their structure on the atomic level with chemical sensitivity. Using aberration-corrected scanning transmission electron microscopy in combination with atomic-resolution electron energy-loss spectroscopy, we show that the controversial structural arrangement of the $Fe_2O_{2+\delta}$ layers in the mixed ionic-electronic conducting $Sr_4Fe_6O_{12+\delta}$ perovskite can be unambiguously resolved. Our results provide direct experimental evidence for the presence of a nanomixture of "ordered" and "disordered" domains in an epitaxial $Sr_4Fe_6O_{12+\delta}$ thin film. The most favorable arrangement is the disordered structure and is interpreted as a randomly occurring but well-defined local shift of the Fe—O chains in the $Fe_2O_{2+\delta}$ layers. By analyzing the electron energy-loss near-edge structure of the different building blocks in the $Sr_4Fe_6O_{12+\delta}$ unit cell we find that the mobile holes in this mixed ionic-electronic conducting oxide are highly localized in the $Fe_2O_{2+\delta}$ layers, which are responsible for the oxide-ion conductivity. A possible link between disorder and oxygen-ion transport along the $Fe_2O_{2+\delta}$ layers is proposed by arguing that the disorder can effectively break the oxygen diffusion pathways.

KEYWORDS: modulated structure · oxygen-deficient perovskite · mixed ionic-electronic conducting oxide · ferrite · electron energy-loss spectroscopy · scanning transmission electron microscopy

Perovskites exhibiting mixed ionic-electronic conducting properties are being extensively researched as key components in advanced energy applications. Especially interesting for high-temperature applications, such as cathodes in solid oxide fuel cells, are perovskite-related oxides exhibiting different structural blocks due to their superior phase stability. Among them, the oxygen-deficient perovskite compounds with the general formula $A_4B_6O_{12+\delta}$ have been extensively studied over the past decade on account of their complex mechanism of anion nonstoichiometry. Up to now, two representatives of this family are known: the $Sr_4Fe_6O_{12+\delta}$ and the $Ba_4In_{6-x}Mg_xO_{12+\delta}$ solid solutions.[1−7]

The $A_4B_6O_{12+\delta}$ structure is built up of AO and BO_2 perovskite-type layers alternating along the *b*-direction with double $B_2O_{2+\delta}$ layers of 5-fold B polyhedra (Figure 1). The BO_5 polyhedra are arranged within the double layers in bands consisting of double edge-sharing trigonal bipyramids and bands of edge-sharing tetragonal pyramids with variable thickness. These two types of bands are connected to each other by sharing corners. Because of a strong deviation of the shape of these polyhedra from perfect trigonal bipyramidal or tetragonal pyramidal, the assignment of a specific geometry has been the focus of extensive discussions.[1,4,5] Nevertheless, it is widely accepted that with varying oxygen content the coordination number of the B-cations does not change. Instead, variation of the oxygen content is accommodated by changing the thickness

©2013 American Chemical Society

of the bands consisting of tetragonal pyramids, that is, by changing the ratio between edge- and corner-sharing BO_5 polyhedra. Thus, varying the oxygen content in these phases changes the polyhedral sequence in the $B_2O_{2+\delta}$ layers along the *a*-direction resulting in the formation of incommensurately modulated structures. These incommensurate modulations were first identified in $Sr_4Fe_6O_{12+\delta}$ thin films using electron diffraction.[2] By applying a combination of electron diffraction data and high-resolution transmission electron microscopy (HRTEM) imaging, structural models for the $Sr_4Fe_6O_{12+\delta}$ phases were proposed in which a modulation vector $\mathbf{q} = \alpha\mathbf{a}^*$ was identified to change with δ, so that $\delta = 2\alpha$.[2,4] The exact configuration of the modulated $Fe_2O_{2+\delta}$ double layers was later determined from single-crystal X-ray diffraction data.[5] However, X-ray diffraction data also evidenced the presence of diffuse scattering along the stacking direction $\mathbf{b}^*$. This phenomenon was suggested to be caused by a stacking disorder of the $Fe_2O_{2+\delta}$ double layers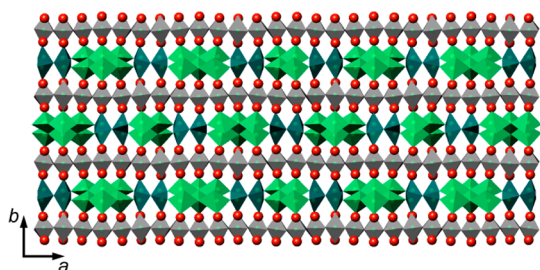.[5] Indeed, different stacking sequences were also observed in the $Sr_4Fe_6O_{12+\delta}$ solid solution by HRTEM imaging,[4] but the exact stacking scheme of the $Fe_2O_{2+\delta}$ layers was difficult to derive due to the possibility of image delocalization affecting phase contrast micrographs in conventional high-resolution electron microscopes. Thus, despite the fact that there is clear evidence of local ordering in the $Fe_2O_{2+\delta}$ layers, the exact atomic stacking structure of the $Sr_4Fe_6O_{12+\delta}$ phases is not yet fully understood.

Here, we investigate the *local* crystal and electronic structure, and the structural defects of a $Sr_4Fe_6O_{12+\delta}$ film employing high-resolution aberration corrected scanning transmission electron microscopy (STEM) and electron energy-loss spectroscopy (EELS). Because of the incoherent nature of the signal, high-angle annular dark-field (HAADF) STEM imaging provides directly interpretable and chemically sensitive images. Besides, as STEM can be combined with EELS to map the elemental distribution at atomic resolution, STEM-EELS has become a powerful tool to study the structure of materials,[8−10] and to characterize defects[11−15] and interfaces[16−18] on the atomic scale.

Figure 1. $Sr_4Fe_6O_{12+\delta}$ ($\delta = 0.74$) **crystal structure viewed along [001]. The Sr atoms are shown as red spheres and the Fe atoms are found in the shaded polyhedra. Perovskite-type layers of gray FeO_6 octahedra alternate along the *b*-direction with double $Fe_2O_{2+\delta}$ layers of FeO_5 polyhedra. Double trigonal bipyramids are shown in dark green and double and triple tetragonal pyramids in light green.**

RESULTS AND DISCUSSION

The (010)-oriented epitaxial $Sr_4Fe_6O_{12+\delta}$ (SFO) film was deposited on a $SrTiO_3$(001) substrate by pulsed laser deposition.[19] Details about the deposition conditions can be found in the Methods section. Figure 2a shows a HAADF-STEM image of the film/substrate interface. The HAADF signal (95−195 mrad) scales approximately with the square of the atomic number Z. Thus, the HAADF image of Figure 2a is dominated by the Sr, Fe, and Ti cations, and to a lesser degree, by the O atoms. At the SFO/$SrTiO_3$ interface a ∼2.5-nm-thick layer with perovskite structure and a HAADF image intensity very close to the one of the SFO film can be observed (Figure 2a). Therefore, its composition can
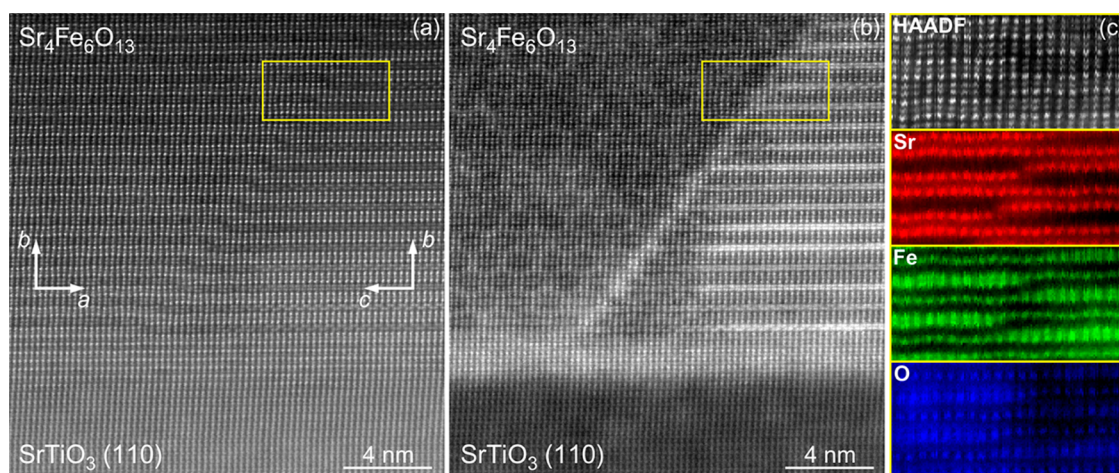

Figure 2. Antiphase boundary in a SFO film on a $SrTiO_3$ substrate. The presence of a $SrFeO_{3-x}$ buffer layer of higher intensity promotes the formation of an antiphase boundary. (a, b) Cross-sectional HAADF- and ADF-STEM images of the SFO/$SrTiO_3$(001) interface, respectively. (c) Simultaneous HAADF image and atomic-resolution maps of the Sr $M_{4,5}$, Fe $L_{2,3}$ and O K edges calculated from the EELS images obtained from the area outlined with a yellow square in panels a and b.

safely be ascribed to SrFeO$_{3-x}$. Similar perovskite-type buffer layers were previously observed in SFO films grown on SrTiO$_3$ and NdGaO$_3$ substrates.[20] It was suggested that during the growth process the first deposited layers mimic the perovskite stacking of the substrate and a perovskite buffer layer with limited thickness is formed instead of the stable SFO phase. In the present case the buffer layer thickness is not constant and it oscillates between 6 and 7 perovskite unit cells. Therefore, steps on the SrFeO$_{3-x}$ layer surface are created promoting the formation of anti-phase boundaries (APBs) in the SFO film. These defects extending to the film surface with an inclination of ∼53° are frequently observed. In the particular case of Figure 2, the APB acts also as a permutation boundary, that is, a twin boundary with a supplementary translation vector. Across the permutation boundary the a- and c-axes are swapped leaving the b-axis unchanged. In Figure 2a, the visible repeat period along the out-of-plane b-axis corresponds to the -SrO-FeO$_2$-SrO-Fe$_2$O$_{2+\delta}$-SrO- sequence of alternating layers. However, from the HAADF image of Figure 2a it is hard to distinguish the [001] domain from the [100] domain at each side of the APB. This becomes clear when inspecting the annular dark field (ADF) STEM image of Figure 2b, which was recorded simultaneously with the HAADF-STEM image. The ADF signal (41−95 mrad) is more sensitive to diffraction contrast and to any effect that leads to a dechannelling of the incident electron beam.[21,22] Therefore, strain fields from oxygen vacancies are readily detected by ADF imaging through the associated displacements of the adjacent cation sites and the subsequent dechannelling of the electron beam from the cation columns.[23] Indeed, at the left side and at the lower right side of the APB, the characteristic modulation of the Fe$_2$O$_{2+\delta}$ layers along the a-axis is clearly visible as a hexagonal pattern (this pattern reproduces the polyhedral sequence shown in the model of Figure 1). The satellite reflections generated by this modulation are used to determine the oxygen composition of the film. The experimentally measured $\alpha = 0.37$ component of the modulation vector allows us to derive a Sr$_4$Fe$_6$O$_{12.74}$ film composition following the relation $\delta = 2\alpha$ given in reference 2.

The formation of APBs may impact the oxide-ion conductivity of the films which is assumed to be strictly two-dimensional, confined to the Fe$_2$O$_{2+\delta}$ double layers.[24−26] To understand the structure of the APBs and their influence on the conducting properties of epitaxial SFO thin films, we performed atomic-resolution EELS mapping of the elements at the vicinity of the APB. Such an EELS image was collected from the marked yellow region in Figure 2a,b by using a dedicated aberration-corrected scanning transmission electron microscope operated at 100 kV (for details see Methods section). After noise reduction by principal component analysis (PCA) using multivariate statistical
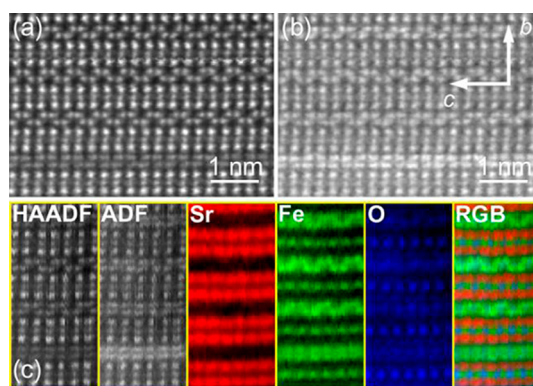

Figure 3. Atomic-resolution chemical imaging of SFO along the [100] direction. (a, b) High-resolution HAADF- and ADF-STEM images, respectively. (c) Simultaneous HAADF and ADF images and elemental atomic-resolution maps calculated from the EELS images. The RGB map is generated using red for Sr, green for Fe, and blue for O.

analysis,[27] the background in all spectra was subtracted by fitting a decaying power-law function to an energy window just in front of the different core-loss edge onsets. Figure 2c shows the elemental atomic-resolution maps of the Sr $M_{4,5}$, Fe $L_{2,3}$, and O K edges extracted from the spectrum image together with the simultaneously acquired HAADF image. It is noteworthy that the resolution of the EELS map even enables to resolve the adjacent Fe atomic columns of the Fe$_2$O$_{2+\delta}$ double layers separated by a projected distance of ∼1.5 Å along the b-axis. The EELS data reveal that the APB interrupts the lateral continuity of only one-half of the SrO layers. On the other hand, all Fe$_2$O$_{2+\delta}$ double layers are laterally interrupted and connected to FeO$_2$ perovskite-type layers and *vice versa*. Therefore, we can anticipate that the presence of APBs with a translation vector $R \approx 1/5[010]_b$ will have a negative impact on the oxide-ion conductivity of the SFO films. It should be noted that APBs with a similar atomic arrangement are present in the bulk Tl- and Pb-doped SFO systems, forming in the latter case an unusual terrace-like structure.[28,29]

Another striking feature can be observed in the [100] domain displayed in the ADF image of Figure 2b: successive double Fe$_2$O$_{2+\delta}$ layers show substantial intensity variations. Figure 3 panels a and b show a HAADF- and the corresponding ADF-STEM image of four double layers imaged along the [100] direction. The Fe atoms of the three upper double layers are arranged in a zigzag pattern delimited by brighter Sr atomic columns (Figure 3a) while in the lower double layer the zigzag pattern is blurred. This layer appears brighter in the ADF image of Figure 3b indicating different channeling conditions caused by a distinct atomic reconstruction. Elemental maps extracted from an EELS image obtained from the same area (Figure 3c) prove that the Fe atomic columns in the lower layer are disordered when compared to the three upper double layers.
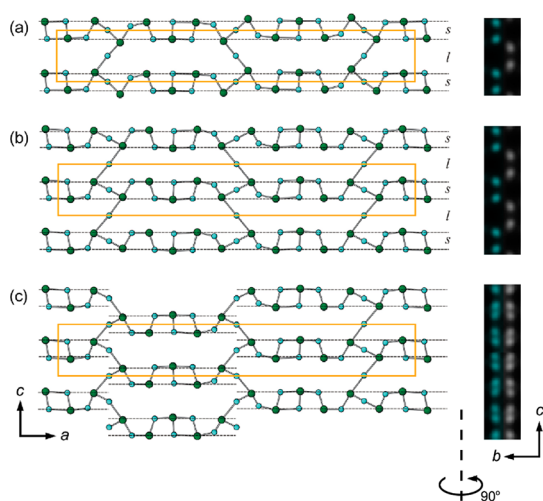
Figure 4. Structure of the $Fe_2O_{2+\delta}$ double layer: the $FeO_{1+\delta/2}$ sublayers. (a) Model of an "ordered" $FeO_{1+\delta/2}$ sublayer consisting of Fe−O atoms linked through extra oxygens. The chains run along the a-direction and are marked with dashed lines. The Fe atoms are shown as larger green spheres and the O atoms as smaller blue spheres. The short and long separations between the chains along the c-axis are marked as s and l, respectively. The unit cell of the commensurate approximant is outlined with an orange rectangle. (b) The -s-l-s-l-s- pattern in this "ordered" sublayer is shifted by $c/2$ with respect to the one in panel a (see orange rectangle). (c) $FeO_{1+\delta/2}$ sublayer representing a mixed "disordered" configuration, where a fragment of the layer in panel a is inserted into the matrix of the layer in panel b. At the right side of the models, simulated HAADF-STEM images of the corresponding $Fe_2O_{2+\delta}$ double layers are included. The atomic columns highlighted in green in the HAADF-STEM images are obtained by projecting all the Fe and O atoms shown in the models along the a-direction. The -s-l-s- and the -s-l-s-l-s- patterns of Figure 2a,b are readily observable in the corresponding HAADF-STEM images, while the sequence is lost for the "disordered" configuration of Figure 4c.

To build possible models for the ordered and disordered variants, we adopted the local atomic arrangements of the $Fe_2O_{2+\delta}$ layer derived from the incommensurately modulated $Sr_4Fe_6O_{12+\delta}$ structure refined from single-crystal X-ray diffraction data.[5] Each $Fe_2O_{2+\delta}$ layer can be considered as a pair of adjacent $FeO_{1+\delta/2}$ layers. The $FeO_{1+\delta/2}$ layers are in turn composed of Fe−O columns running along the a-axis (Figure 4). Along the c-axis the chains are separated by short (s) and long (l) distances. Figure 4 panels a and b show identical configurations of the adjacent $FeO_{1+\delta/2}$ layers but with the ordered pattern of alternating s and l separations shifted by $c/2$ (this can be seen from the orange rectangles outlining the unit cells in both figures). Being viewed along [100], such ordering results in a zigzag arrangement of the projected Fe−O columns. The disordered arrangement arises if the ...s-l-s-l-s... pattern is locally violated by insertion of a fragment shifted by $c/2$ and mirrored with respect to the (001) plane, as is shown, for example, in Figure 4c. This mixed configuration causes the apparent disorder in the projected Fe−O columns observed in the [100] STEM images. The HAADF images shown in Figure 5a,b are obtained from two different
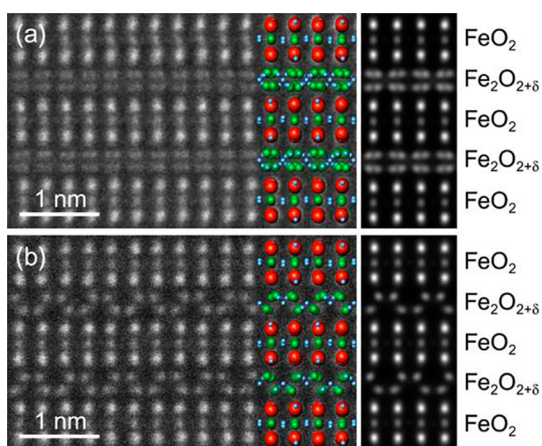

Figure 5. Atomic reconstructions of the $Fe_2O_{2+\delta}$ layers in SFO along [100]. (a) Experimental HAADF-STEM image of the disordered $Sr_4Fe_6O_{12+\delta}$ structure (left) with the mixed $Fe_2O_{2+\delta}$ layers (as in Figure 4c) and calculated image for a 12-nm-thick crystal (right). (b) Experimental HAADF-STEM image of the $Sr_4Fe_6O_{12+\delta}$ structure (left) with the ordered $Fe_2O_{2+\delta}$ layers (as in Figure 4a,b) and calculated image for a 12-nm-thick crystal (right). The corresponding structural models are overlaid on the experimental images (Sr = red, Fe = green, O = blue). The original micrographs are shown in the Supporting Information Figures S1 and S2.

areas exhibiting respectively a disordered and a zigzag arrangement of the $Fe_2O_{2+\delta}$ layers. The crystal structure models of both variants were obtained from the commensurate $\mathbf{q} = \alpha\mathbf{a}^* = {}^3/_7\mathbf{a}^* \approx 0.43\mathbf{a}^*$ approximants of the modulated $Sr_4Fe_6O_{12+\delta}$ structure,[5] adopting the corresponding subgroup allowing for an ordered ...s-l-s-l-s... alternation of the separations between the Fe−O chains. The excellent match between the experimental and the calculated HAADF images (Figure 5a,b) confirms the proposed structure models of the ordered and disordered $Fe_2O_{2+\delta}$ layers. Furthermore, consecutive ordered $Fe_2O_{2+\delta}$ layers are seen to pile up following two different stacking configurations as shown in Figures 3a and 5b. While no shift along the c-axis is observed between the consecutive zigzag layers of Figure 3a, the zigzag layers of Figure 5b are shifted by $c/2$ making the zigzag layers appear mirrored with respect to a (010) plane located at the center of the perovskite-type layer.

For bulk $Sr_4Fe_6O_{12+\delta}$ ceramics the oxygen ionic conductivity at 1173 K varies between $\sim6 \times 10^{-4}$ and $\sim3 \times 10^{-4}$ S·cm^{-1} for partial oxygen pressures $p(O_2) = 10{-}1 \times 10^5$ Pa.[30] Low oxygen ionic conductivity was also found for epitaxial $Sr_4Fe_6O_{12+\delta}$ thin films on $NdGaO_3$, $LaAlO_3$ and $SrTiO_3$ substrates, being below the measurable limit.[31] It was noticed that such low ionic conductivity is not in line with *ab initio* computations and with the ionic conductivity in other similar structures such as the $Sr_2Fe_2O_5$ brownmillerite[32−35] admitting that the origin of this apparent discrepancy is not yet clear and may be associated with blocking effects of the grain boundaries in polycrystalline ceramic materials. The observed mixed configuration of the $Fe_2O_{2+\delta}$ layers
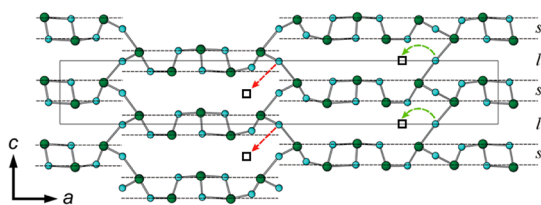
Figure 6. Possible oxygen migration pathways along the $FeO_{1+\delta/2}$ sublayers. Green arrows indicate the oxygen jumps to the closest interstitial position in the ordered layer; red arrows indicate the pathway in the layer with mixed configuration.

Figure 7. Oxygen K-edge (left) and iron L-edge (right) spectra of the perovkite-type FeO_2 layers, and the double $Fe_2O_{2+\delta}$ layers. The FeO_2 spectra are averaged from 30 spectra while the $Fe_2O_{2+\delta}$ spectra are averaged from 45 spectra. Inset: enlarged view of the prepeak region A.

provides an alternative possible explanation for the low oxygen-ion transport through the $Sr_4Fe_6O_{12+\delta}$ structure.

It is assumed that the migration of the ion charge carriers in $Sr_4Fe_6O_{12+\delta}$, both by oxygen vacancies and interstitials, occurs along the $Fe_2O_{2+\delta}$ layers.[24−26] Both migration of oxygen vacancies and interstitial diffusion are believed to contribute to the total ionic conductivity of this material. At low partial oxygen pressures $[p(O_2) < 10^5$ Pa] the ionic conductivity is dominated by the migration of oxygen vacancies, whereas at higher $p(O_2) > 10^5$ Pa the oxygen transport occurs through oxygen interstitials.[30] The atomic arrangement within the $FeO_{1+\delta/2}$ sublayers provides the native paths for the migration of the oxygen interstitials: it consists of a jump of the oxygen atom along the l channel into a neighboring interstitial position, coordinated by two Fe atoms (marked with green arrows in Figure 6). In the uniform $FeO_{1+\delta/2}$ sublayers infinite chains of interstitial positions are available and the migration can occur at a relatively low energy cost. However, introducing a mixed configuration with a fragment shifted by $c/2$ effectively breaks this diffusion pathway. The distance between the O atom and the next available interstitial position becomes $\sim\sqrt{2}$ times larger (red arrows in Figure 6) and a bottleneck of two closely positioned oxygen atoms additionally prevents the oxygen transfer. This qualitative picture, essentially based on geometrical considerations, implies that the disorder in the $Fe_2O_{2+\delta}$ layers could deteriorate the oxide ion transport. Careful control of the synthesis conditions might diminish the degree of this disorder and its potential negative effect.

Information about the bonding and coordination of the Fe atoms was obtained by analyzing the electron energy-loss near-edge structure (ELNES) of the different layers in the SFO unit cell. Figure 7 shows the O K-edge and Fe $L_{2,3}$-edge EELS spectra acquired from the two different building blocks present in SFO, that is, the perovskite-type layers and the double $Fe_2O_{2+\delta}$ layers. Smart Acquisition linescans[36,37] were run along the stacking direction crossing several FeO_2 and $Fe_2O_{2+\delta}$ layers (for details see the Methods section). Thus, the experimental results reflect the integral of all possible oxygen and iron environments in each layer. The EELS spectra were background subtracted for each core-loss edge and no PCA processing was applied.
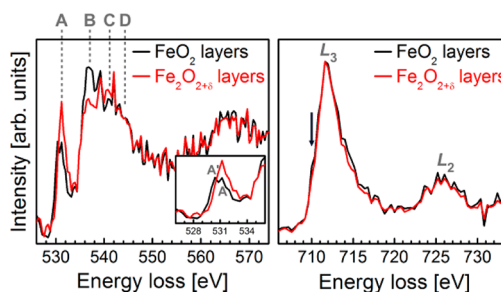
The ELNES of the O K-edge spectra can be divided into two regions: the prepeak region from $\sim$528 to $\sim$534 eV and the postedge region from $\sim$534 to $\sim$548 eV. The prepeak region is characterized by the presence of a well-defined peak at 531.2 eV (labeled A) in both spectra and by an additional low-energy peak at 530.4 eV (labeled A′) in the FeO_2 spectrum; see the inset in Figure 7. The postedge region of the FeO_2 layers shows three well-separated features at 536.5 eV (labeled B), 541 eV (labeled C), and 544 eV (labeled D), while the $Fe_2O_{2+\delta}$ layer spectrum is characterized by a B peak maximum followed by a much lower D peak.

As EELS is comparable to X-ray absorption spectroscopy (XAS), in that X-rays produce similar ionization processes to those induced by the electron beam in the TEM, we compared our experimental spectra with XAS and EELS data from $SrFeO_3$,[38] and other iron oxides.[39−41] We found that peak A stems from transitions to hybridized O 2p−Fe 3d orbitals, while the postedge region of the spectra is attributed to hybridization between the O 2p and Fe 4sp states. The observed differences in the postedge fine structure of the FeO_2 and $Fe_2O_{2+\delta}$ spectra reveal the different site coordination of the Fe atoms which is determined by the nearest oxygen neighbors. Besides, the splitting of the prepeak region of the perovskite-type FeO_2 layer spectrum by 0.8 eV (see the inset in Figure 7) indicates that the 3d orbital states further split into t_{2g} and e_g levels by octahedral ligand-field splitting. A striking difference between the spectra of the FeO_2 and $Fe_2O_{2+\delta}$ layers is also found on the relative intensity of the A and B peaks. While the intensity of these peaks is very similar for the $Fe_2O_{2+\delta}$ layer spectrum (red), the B peak intensity is almost twice the intensity of the A peak for the FeO_2-layer spectrum (black). Previous studies showed that the prepeak can be used to estimate the density of hole states.[42,43] Therefore, the higher prepeak in the $Fe_2O_{2+\delta}$-layer spectrum indicates a higher concentration of mobile holes in the double-layers. This is in good agreement with previously reported electron−hole conductivity measurements in epitaxial SFO film which showed that the

conductivity of the films can be tailored by changing the oxygen content in the double layers.[44]

In comparison, changes in the fine structure of the Fe $L_{2,3}$-edge are far more subtle (Figure 7). The spectra consist of two "white line" peaks which are separated by ~13 eV due to the spin−orbit splitting of the Fe 2p core hole. Besides, the FeO_2-layer spectrum (black) shows a shoulder (at 710 eV) on the left side of the L_3 maximum due to the t_{2g}−e_g crystal field splitting of the octahedral coordination. In the data acquired from the nonperovskite $Fe_2O_{2+\delta}$ layers (red) on the other hand, the shoulder is hardly visible in the L_3 peak, which makes it appear narrower. The lack of fine structures in the Fe $L_{2,3}$-edge of the double layers might be caused by the overlapping between the 3d states arising from the various distorted pentacoordinated geometries of the iron atoms. No significant relative intensity changes of the L_3 and L_2 white lines are observable in the experiments confirming that the oxidation state of Fe is equivalent in both types of layers.

CONCLUSIONS

By using aberration-corrected HAADF- and ADF-STEM imaging combined with EELS at atomic resolution, we have demonstrated that the double $Fe_2O_{2+\delta}$ layers in the SFO structure may adopt different atomic arrangements. Our results provide direct experimental evidence for the simultaneous presence of areas exhibiting different atomic reconstructions of the $Fe_2O_{2+\delta}$ layers. In the most favorable arrangement a "disordered" structure is ascertained. The spatial arrangement of the Fe and O atoms in the "disordered" layers is derived from the incommensurately modulated $Sr_4Fe_6O_{12+\delta}$ structure[5] as a locally occurring shift of the Fe−O chains in the $Fe_2O_{2+\delta}$ layers. "Ordered" atomic reconstructions of the $Fe_2O_{2+\delta}$ layers are also observed over relatively large local areas. By comparing our high-resolution STEM experimental data with multislice image calculations, we corroborate the proposed structural models. We have also shown that the different coordination environment for the Fe atoms in the perovskite-type layers and the double $Fe_2O_{2+\delta}$ layers results in clear differences in the near-edge fine structure of the O K-edge. Thus, the observed differences in the relative intensity of the O K-edge prepeak indicate a higher mobile-hole concentration in the double layers. Therefore the presence of APBs, which laterally transform $Fe_2O_{2+\delta}$ layers into FeO_2 perovskite-type layers and vice versa, is likely to have a deleterious effect on both the electron−hole and the oxide−ion conduction of the films. Even a more striking negative effect on the ionic conductivity can be expected from the mixed configuration of the $Fe_2O_{2+\delta}$ layers which effectively breaks the pathways for the interstitial diffusion. The results we present clarify the exact atomic stacking structure of the $Sr_4Fe_6O_{12+\delta}$ phases and evidence STEM-EELS is a valuable complementary technique to X-ray diffraction when determination of a crystal structure is hindered by the presence of disorder-related diffuse scattering.

METHODS

Sample Preparation. The epitaxial $Sr_4Fe_6O_{12+\delta}$ (SFO) thin film was grown on a polished (001) oriented $SrTiO_3$ substrate by pulsed laser deposition using a Nd:YAG laser with tripled frequency (355 nm wavelength), 9 ns pulse length, 10 Hz repetition rate, and 2−3 J/cm^2 energy density per pulse. The target for the ablation experiment was prepared by a solid-state reaction from a stoichiometric mixture of $SrCO_3$ and Fe_2O_3. The resultant powder was milled, uniaxially pressed into pellets, and finally sintered in air at 1150 °C. X-ray diffraction measurements confirmed that the target was the single phase $Sr_4Fe_6O_{13\pm\delta}$, as determined by Yoshiasa et al.[1] During deposition, the substrate temperature was kept at 750 °C and the oxygen pressure in the chamber was settled at 3×10^{-2} mbar. After the sample was deposited, it was cooled at 10 °C/min under the same atmosphere. Details of the X-ray diffraction studies and scanning electron microscopy are found in Pardo et al.[19] Samples for TEM were prepared in cross-section geometry; the samples were cut parallel to the (110) planes of the $SrTiO_3$ substrate and mechanically ground with a tripod polisher to a thickness of about 20 μm, followed by final liquid nitrogen-cooled ion milling under grazing incidence until electron transparency.

Instrumentation. The EELS data in this study was obtained at 100 kV on a Nion UltraSTEM 100 microscope equipped with a C_5 Nion quadrupole−octupole-type probe aberration corrector and an ultrahigh vacuum Gatan Enfina spectrometer. The convergence and collection semiangles were set to 30.5 and 33 mrad, respectively. For these values, the energy resolution measured as the full width at half-maximum of the zero-loss peak is ~0.35 eV. Yet, in order to cover a large energy range in EELS, the dispersion was set to 1 eV/channel for the spectrum

images in Figures 2 and 3. No drift correction during acquisition was used in this work. Energy windows of 50 eV were used to form the EELS images of the Sr-$M_{4,5}$, Fe-$L_{2,3}$, and O-K edges. To resolve the near-edge fine structure of the core-loss edges of Figure 7 the dispersion was set to 0.2 eV/channel. In typical operating conditions for the experiments described in this paper, the microscope provides an estimated spatial resolution of 0.85 Å. The annular semidetection range of the annular dark-field detector was set to collect electrons scattered between 95 and 195 mrad for the HAADF images and between 41 and 95 mrad for the ADF images (when used at the same time as the HAADF detector). HAADF-STEM in Figure 5 was carried out using the aberration-corrected TEAM 0.5 microscope operated at 300 kV. The TEAM 0.5 microscope[45] is a modified FEI Titan 80−300 equipped with a Schottky-type high-brightness field-emission electron source and an improved hexapole-type illumination spherical aberration (C_S) corrector.[46] A probe convergence angle of ~19 mrad was set yielding a calculated probe size of about 65 pm. The annular semidetection range of the annular dark-field detector was calibrated at 80−300 mrad.

Image Simulations. High-resolution STEM image simulations were carried out using the xHREM simulation package.

Conflict of Interest: The authors declare no competing financial interest.

REFERENCES AND NOTES

1. Yoshiasa, A.; Ueno, K.; Kanamaru, F.; Horiuchi, H. Structure of $Sr_4Fe_6O_{13}$, A New Perovskite-Derivative in the Sr—Fe—O System. *Mater. Res. Bull.* **1986**, *21*, 175–181.

2. Rossell, M. D.; Abakumov, A. M.; Van Tendeloo, G.; Pardo, J. A.; Santiso, J. Structure and Microstructure of Epitaxial $Sr_4Fe_6O_{12+\delta}$ Films on $SrTiO_3$. *Chem. Mater.* **2004**, *16*, 2578–2584.

3. Mellenne, B.; Retoux, R.; Lepoittevin, C.; Hervieu, M.; Raveau, B. Oxygen Nonstoichiometry in $Sr_4Fe_{12}O_{26}$: The Derivatives $[Sr_8Fe_{12}O_{26}]\cdot[Sr_2Fe_3O_6]_n$. *Chem. Mater.* **2004**, *16*, 5006–5013.

4. Rossell, M. D.; Abakumov, A. M.; Van Tendeloo, G.; Lomakov, M. V.; Istomin, S. Y.; Antipov, E. V. Transmission Electron Microscopic Study of the Defect Structure in $Sr_4Fe_6O_{12+\delta}$ Compounds with Variable Oxygen Content. *Chem. Mater.* **2005**, *17*, 4717–4726.

5. Pérez, O.; Mellenne, B.; Retoux, R.; Raveau, B.; Hervieu, M. A New Light on the Iron Coordination in $Sr_4Fe_6O_{13\pm\delta}$: Super Space Formalism and Structural Mechanism. *Solid State Sci.* **2006**, *8*, 431–443.

6. Kanamaru, F.; Koizuni, M. Synthesis of $Ba_4In_6O_{13}$. *J. Am. Ceram. Soc.* **1973**, *56*, 399–400.

7. Abakumov, A. M.; Rossell, M. D.; Gutnikova, O. Y.; Drozhzhin, O. A.; Leonova, L. S.; Dobrovolsky, Y. A.; Istomin, S. Y.; Van Tendeloo, G.; Antipov, E. V. Superspace Description, Crystal Structures, and Electric Conductivity of the $Ba_4Fe_{6-x}Mg_xO_{13-x/2}$ Solid Solutions. *Chem. Mater.* **2008**, *20*, 4457–4467.

8. Trasobares, S.; López-Haro, M.; Kociak, M.; March, K.; de La Peña, F.; Perez-Omil, J. A.; Calvino, J.; Lugg, N. R.; D'Alfonso, A. J.; Allem, L. J.; *et al.* Chemical Imaging at Atomic Resolution as a Technique to Refine the Local Structure of Nanocrystals. *Angew. Chem., Int. Ed.* **2011**, *50*, 868–872.

9. Pennycook, T. J.; Oxley, M. P.; Garcia-Barriocanal, J.; Bruno, F. Y.; Leon, C.; Santamaria, J.; Pantelides, S. T.; Varela, M.; Pennycook, S. J. Seeing Oxygen Disorder in YSZ/SrTiO_3 Colossal Ionic Conductor Heterostructures Using EELS. *Eur. Phys. J. Appl. Phys.* **2011**, *54*, 33507.

10. Rossell, M. D.; Erni, R.; Prange, M. P.; Idrobo, J. C.; Luo, W.; Zeches, R. J.; Pantelides, S. T.; Ramesh, R. Atomic Structure of Highly Strained $BiFeO_3$ Thin Films. *Phys. Rev. Lett.* **2012**, *108*, 047601.

11. Gunawan, L.; Lazar, S.; Gautreau, O.; Harnagea, C.; Pignolet, A.; Botton, G. A. Locating La Atoms in Epitaxial $Bi_{3.25}La_{0.75}Ti_3O_{12}$ Films through Atomic Resolution Electron Energy Loss Spectroscopy Mapping. *Appl. Phys. Lett.* **2009**, *95*, 192902.

12. MacLaren, I.; Wang, L. Q.; Schaffer, B.; Ramasse, Q. M.; Craven, A. J.; Selbach, S. M.; Spaldin, N. A.; Miao, S.; Kalantari, K.; Reaney, I. M. Novel Nanorod Precipitate Formation in Neodymium and Titanium Codoped Bismuth Ferrite. *Adv. Funct. Mater.* **2013**, *23*, 683–689.

13. Abou-Ras, D.; Schaffer, B.; Schaffer, M.; Schmidt, S. S.; Caballero, R.; Unold, T. Direct Insight into Grain Boundary Reconstruction in Polycrystalline Cu(In,Ga)Se$_2$ with Atomic Resolution. *Phys. Rev. Lett.* **2012**, *108*, 075502.

14. Rossell, M. D.; Ramasse, Q. M.; Findlay, S. D.; Rechberger, F.; Erni, R.; Niederberger, M. Direct Imaging of Dopant Clustering in Metal-Oxide Nanoparticles. *ACS Nano* **2012**, *6*, 7077–7083.

15. Detemple, E.; Ramasse, Q. M.; Sigle, W.; Cristiani, G.; Habemeier, H.-U.; Keimer, B.; van Aken, P. A. Ruddlesden-Popper Faults in $LaNiO_3/LaAlO_3$ Superlattices. *J. Appl. Phys.* **2012**, *112*, 013509.

16. Muller, D. A.; Kourkoutis, L. F.; Murfitt, M.; Song, J. H.; Hwang, H. Y.; Silcox, J.; Dellby, N.; Krivanek, O. L. Atomic-Scale Chemical Imaging of Composition and Bonding by Aberration-Corrected Microscopy. *Science* **2008**, *319*, 1073–1076.

17. Pennycook, S. J.; Borisevich, A. Y.; Varela, M.; Lupini, A. R.; Chang, H. J.; Leonard, D. N.; Pennycook, T. J.; Oxley, M. P.; Idrobo, J. C.; Yurdakul, H.; *et al.* Interface Structure-Property Relations through Aberration-Corrected STEM. *Microsc. Microanal.* **2010**, *16*, 1420–1421.

18. Shah, A. B.; Ramasse, Q. M.; Zhai, X.; Wen, J. G.; May, S. J.; Petrov, I.; Bhattacharya, A.; Abbamonte, P.; Eckstein, J. N.; Zuo, J.-M. Probing Interfacial Electronic Structures in Atomic Layer $LaMnO_3$ and $SrTiO_3$ Superlattices. *Adv. Mater.* **2010**, *22*, 1156–1160.

19. Pardo, J. A.; Santiso, J.; Solís, C.; Garcia, G.; Figueras, A.; Rossell, M. D.; Van Tendeloo, G. Epitaxial $Sr_4Fe_6O_{13\pm\delta}$ Films Obtained by Pulsed Laser Deposition. *J. Cryst. Growth* **2004**, *262*, 334–340.

20. Solís, C.; Rossell, M. D.; Garcia, G.; Van Tendeloo, G.; Santiso, J. Unusual Strain Accommodation and Conductivity Enhancement by Structure Modulation Variation in $Sr_4Fe_6O_{12+\delta}$ Epitaxial Films. *Adv. Funct. Mater.* **2008**, *18*, 785–793.

21. Perovic, D. D.; Rossow, C. J.; Howie, A. Imaging Elastic Strains in High-Angle Annular Dark-Field Scanning-Transmission Electron Microscopy. *Ultramicroscopy* **1993**, *52*, 353–359.

22. Hillyard, S. E.; Silcox, J. Detector Geometry, Thermal Diffuse Scattering and Strain Effects in ADF STEM Imaging. *Ultramicroscopy* **1995**, *58*, 6–17.

23. Muller, D. A.; Nakagawa, N.; Ohtomo, A.; Grazul, J. L.; Hwang, H. Y. Atomic-Scale Imaging of Nanoengineered Oxygen Vacancy Profiles in $SrTiO_3$. *Nature* **2004**, *430*, 657–661.

24. Ma, B.; Balachandran, U. Oxygen Nonstoichiometry in Mixed-Conducting $SrFeCo_{0.5}O_x$. *Solid State Ionics* **1997**, *100*, 53–62.

25. Guggilla, S.; Manthiram, A. Crystal Chemical Characterization of the Mixed Conductor $Sr(Fe,Co)_{1.5}O_y$ Exhibiting Unusually High Oxygen Permeability. *J. Electrochem. Soc.* **1997**, *144*, L120–L122.

26. Waerenborgh, J. C.; Avdeev, M.; Patrakeev, M. V.; Kharton, V. V.; Frade, J. R. Redox Behaviour of $Sr_4Fe_6O_{13\pm\delta}$ by Mössbauer Spectroscopy and Neutron Diffraction. *Mater. Lett.* **2003**, *57*, 3245–3250.

27. Watanabe, M.; Okunishi, E.; Ishizuka, K. Analysis of Spectrum-Imaging Datasets in Atomic-Resolution Electron Microscopy. *Microsc. Anal.* **2009**, *23*, 5–7.

28. Lepoittevin, C.; Malo, S.; Pérez, O.; Nguyen, N.; Maignan, A.; Hervieu, M. $Pb_4Sr_{13}Fe_{24}O_{53}$: An Original Terrace Structure, Related to $Sr_{4-x}Pb_xFe_6O_{13-\delta}$. *Solid State Sci.* **2006**, *8*, 1294–1301.

29. Lepoittevin, C.; Malo, S.; Nguyen, N.; Hebert, S.; Van Tendeloo, G.; Hervieu, M. A Layered Iron-Rich 2234-Type with a Mixed Valence of Iron: The Ferrimagnetic Tl-Doped $Fe_2(Sr_{2-\varepsilon}Tl_\varepsilon)Sr_3Fe_4O_{14.65}$. *Chem. Mater.* **2008**, *20*, 6468–6476.

30. Avdeev, M. Y.; Patrakeev, M. V.; Kharton, V. V.; Frade, J. R. Oxygen Vacancy Formation and Ionic Transport in $Sr_4Fe_6O_{13\pm\delta}$. *J. Solid State Electrochem.* **2002**, *6*, 217–224.

31. Solís, C.; Jung, W.; Tuller, H. L.; Santiso, J. Defect Structure, Charge Transport Mechanisms, and Strain Effects in $Sr_4Fe_6O_{12+\delta}$ Epitaxial Thin Films. *Chem. Mater.* **2010**, *22*, 1452–1461.

32. Tarancón, A.; Burriel, M.; Santiso, J.; Skinner, S. J.; Kilner, J. A. Advances in Layered Oxide Cathodes for Intermediate Temperature Solid State Fuel Cells. *J. Mater. Chem.* **2010**, *20*, 3799–3813.

33. Santiso, J.; Burriel, M. Deposition and Characterization of Epitaxial Oxide Thin Films for SOFCs. *J. Solid State Electrochem.* **2011**, *15*, 985–1006.

34. Chroneos, A.; Yildiz, B.; Tarancón, A.; Parfitt, D.; Kilner, J. A. Oxygen Diffusion in Solid Oxide Fuel Cell Cathode and Electrolyte Materials: Mechanistic Insights from Atomistic Simulations. *Energy Environ. Sci.* **2011**, *4*, 2774–2789.

35. Fisher, C. A. J.; Islam, M. S. Mixed Ionic/Electronic Conductors $Sr_2Fe_2O_5$ and $Sr_4Fe_6O_{13}$: Atomic-Scale Studies of Defects and Ion Migration. *J. Mater. Chem.* **2005**, *15*, 3200–3207.

36. Sader, K.; Schaffer, B.; Vaughan, G.; Brydson, R.; Brown, A.; Bleloch, A. Smart Acquisition EELS. *Ultramicroscopy* **2010**, *110*, 998–1003.

37. Heidelmann, M.; Barthel, J.; Houben, L. StripeSTEM, a Technique for the Isochronous Acquisition of High Angle Annular Dark-Field Images and Monolayer Resolved Electron Energy Loss Spectra. *Ultramicroscopy* **2009**, *109*, 1447–1452.

38. Abbate, M.; de Groot, F. M. F.; Fuggle, J. C.; Fujimori, A.; Strebel, O.; Lopez, F.; Domke, M.; Kaindl, G.; Sawatzky, G. A.; Takano, M.; *et al.* Controlled-Valence Properties of $La_{1-x}Sr_xFeO_3$ and $La_{1-x}Sr_xMnO_3$ Studied by Soft-X-ray Absorption Spectroscopy. *Phys. Rev. B* **1992**, *46*, 4511–4519.

39. de Groot, F. M. F.; Grioni, M.; Fuggle, J. C.; Ghijsen, J.; Sawatzky, G. A.; Petersen, H. Oxygen 1s X-ray-Absorption Edges of Transition-Metal Oxides. *Phys. Rev. B* **1989**, *40*, 5715–5723.

40. Colliex, C.; Manoubi, T.; Ortiz, C. Electron-Energy-Loss-Spectroscopy Near-Edge Structures in the Iron−Oxygen System. *Phys. Rev. B* **1991**, *44*, 402–411.

41. Calvert, C. C.; Brown, A.; Brydson, R. Determination of the Local Chemistry of Iron in Inorganic and Organic Materials. *J. Electron Spectrosc. Relat. Phenom.* **2005**, *143*, 173–187.

42. Moodenbaugh, A. R.; Nielsen, B.; Sambasivan, S.; Fisher, D. A.; Friessnegg, T.; Aggarwal, S.; Ramesh, R.; Pfeffer, R. L. Hole-State Density of $La_{1-x}Sr_xCoO_{3-\delta}$ ($0 \leq x \leq 0.5$) Across the Insulator/Metal Phase Boundary. *Phys. Rev. B* **2000**, *61*, 5666–5671.

43. Browning, N. D.; Chisholm, M. F.; Pennycook, S. J.; Norton, D. P.; Lowndes, D. H. Correlation between Hole Depletion and Atomic Structure at High-Angle Grain Boundaries in $YBa_2Cu_3O_{7-\delta}$. *Phys. C* **1993**, *212*, 185–190.

44. Pardo, J. A.; Santiso, J.; Solís, C.; Garcia, G.; Figueras, A.; Rossell, M. D. Thickness-Dependent Transport Properties of $Sr_4Fe_6O_{13}$ Epitaxial Thin Films. *Solid State Ionics* **2006**, *177*, 423–428.

45. Erni, R.; Rossell, M. D.; Kisielowski, C.; Dahmen, U. Atomic-Resolution Imaging with a Sub-50-pm Electron Probe. *Phys. Rev. Lett.* **2009**, *102*, 096101.

46. Müller, H.; Uhlemann, S.; Hartel, P.; Haider, M. Advancing the Hexapole Cs-Corrector for the Scanning Transmission Electron Microscope. *Microsc. Microanal.* **2006**, *12*, 442–455.